Powder Technology 470 (2026) 121957

Contents lists available at ScienceDirect

Powder Technology

journal homepage: www.journals.elsevier.com/powder-technology

A novel method for synthetic packed bed generation considering catalyst pellet fragments

Maximilian Meyer [a,b], Martin Kutscherauer [a], Oliver Richter [b], Maximilian Dochnahl [b], Gerhard Mestl [b], Gregor D. Wehinger [a,*]

[a] Institute of Chemical Process Engineering, Karlsruhe Institute of Technology, Kaiserstraße 12, Karlsruhe, 76131, Baden-Württemberg, Germany
[b] Clariant AG, Waldheimer Straße 15, Bruckmühl-Heufeld, 83052, Bavaria, Germany

HIGHLIGHTS

- New method for synthetic packed bed generation considering catalyst pellet fragments.
- Validation with experimental data of overall bed void fraction and pressure drop.
- PRCFD investigation of the influence of catalyst pellet breakage on pressure drop.

GRAPHICAL ABSTRACT

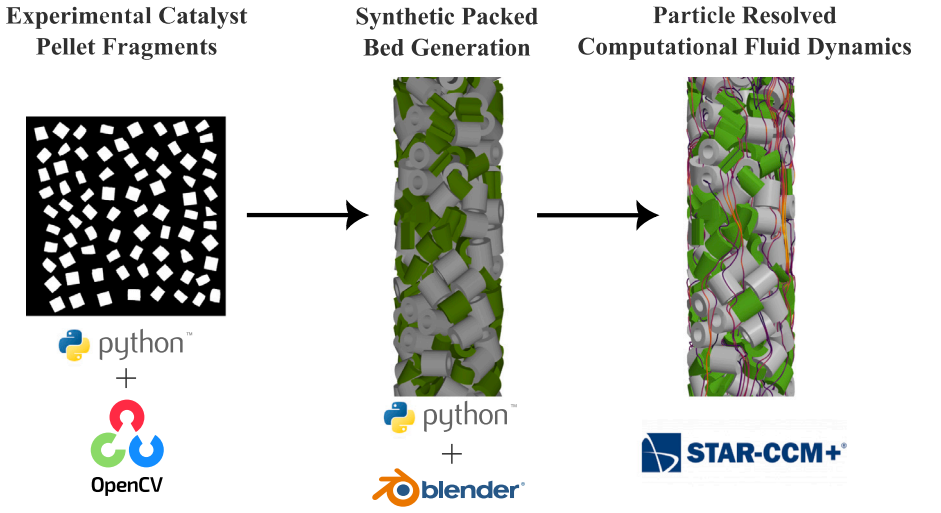

ARTICLE INFO

Keywords:
Packed bed
Pellet breakage
Pressure drop
Packed bed generation
Computational fluid dynamics

ABSTRACT

Random packed bed reactors for heterogeneous catalysis are crucial for the chemical industry. The occurrence of mechanical catalyst pellet failure is commonly known, yet its consequences have hardly been scientifically investigated. To enable a simulative investigation of the influence of catalyst pellet breakage on reactor performance, a novel method for the synthetic generation of packed bed structures is presented. The method consists of the creation of digital particle fragments, the characterization and selection of suitable fragments, as well as the subsequent synthetic packed bed generation. Instead of modeling the breakage process, digital particle fragments are selected prior to the packed bed generation via the PECH$_\alpha$ algorithm. The packed bed generation itself is carried out in the open-source software Blender® 4.0.2 and Python. For the technically relevant range of breakage fractions $(0.0 \leq w_B \leq 0.3)$, sufficient agreement between the overall bed void fractions of synthetic and experimental packed beds was found. Furthermore, flow through those bed structures was simulated with particle-resolved computational fluid dynamics (PRCFD). The pressure drop attained by PRCFD simulations agrees well with the experimental data.

* Corresponding author.
E-mail address: gregor.wehinger@kit.edu (G.D. Wehinger).

https://doi.org/10.1016/j.powtec.2025.121957
Received 20 June 2025; Received in revised form 9 November 2025; Accepted 20 November 2025
Available online 21 November 2025

Nomenclature

Abbreviations

BPL	Bullet Physics Library
CPU	Central Processing Unit
DEM	Discrete Element Method
FDEM	Finite-Discrete Element Method
MAR	Minimal Area Rectangle
PECH	Primal Effective Capacity Heuristic
PRCFD	Particle Resolved Computational Fluid Dynamics
PSD	Particle Size Distribution
RAM	Random-Access Memory
RBA	Rigid Body Approach

Dimensionless numbers

Re_P	Particle Reynolds Number

Greek symbols

α	Greedy coefficient (–)
β	Sliding speed ($m\,s^{-1}$)
δ	Thickness (m)
η	Dynamic viscosity (Pa s)
κ_i	Capacity of dimension i (–)
λ	Size feature distribution (–)
μ_{fric}	Friction coefficient (–)
ν	Kinematic Viscosity ($m^2\,s^{-1}$)
ω	Angular velocity ($rad\,s^{-1}$)
$\overline{\kappa}_i$	Remaining capacity of dimension i (–)
Ψ	Circularity (–)
σ_i	Used capacity of dimension i (–)
τ	Rotational momentum (N m)
ε	Void fraction (–)

Latin symbols

D	Deformation tensor (s^{-1})
e	Unit tensor (–)
T	Viscous stress tensor (Pa)
v	Velocity vector ($m\,s^{-1}$)
$\mathcal{F}$	Friction cone (–)
I	Inertia matrix ($kg\,m^2$)
A	Area (m^2)
a_{ij}	Required capacity of object j in dimension i (–)
b	Width (m)
c_j	Value of object j (–)
d	Diameter (m)
E	Set E (–)
h	Height (m)
$h_{current}$	Current bed height (m)
$h_{dynamic}$	Height of dynamic packed bed section (m)
k_λ	Number of size classes of distribution λ (–)
l	Length (m)
M	Molar mass ($kg\,mol^{-1}$)
m	Mass (kg)
R	Universal gas constant ($J\,K^{-1}\,mol^{-1}$)
r	Radius (m)
U	Perimeter (m)
u_j	Maximum available amount of object j (–)
v	Velocity ($m\,s^{-1}$)
w	Mass fraction (–)
$\overline{u}_j$	Remaining amount of object j (–)
x_j	Decision variables (–)
$\overline{y}_j$	Effective capacity of object j (–)

Super- and subscripts

B	Breakage
BL	Boundary Layer
Br	Fragment
c	Contact
f	Fluid
i	Inner
MAR	Minimal Area Rectangle
nor	Normal
o	Outer
ort	Orthogonal
P	Particle
tan	Tangential

1. Introduction

The vast majority of industrial processes in the chemical industry make use of solid-catalyzed reactions [1]. For the production of large-scale basic chemicals, intermediates and several other applications, fixed-bed reactors are the most important reactor type for heterogeneous catalysis [2,3]. Highly exothermic or endothermic reactions require effective heat transport in or out of the system, which often leads to reactor designs featuring a small tube-to-particle diameter ratio ($d_{i,Tube}/d_P = N < 5$) [4]. Especially for such arrangements, the effects of the local packed bed morphology on fluid flow as well as heat and mass transfer cannot be sufficiently described by conventional pseudo-homogeneous or heterogeneous reactor models [5]. Due to that and the increasing computational power of modern computer architecture, particle resolved computational fluid dynamics (PRCFD) simulations, taking the actual geometric structure into account, are gaining considerable attention in recent years [5]. It is essential that the packed bed morphology used for PRCFD simulations must be as realistic as possible [6,7]. Image-based methods, such as gamma ray tomography or magnetic resonance imaging, can be used to obtain three-dimensional information of packed beds [8,9]. However, they are very time consuming and need special equipment for scanning while synthetic bed generation methods are faster and more flexible in comparison [6].

Apart from thermal and chemical stresses, catalyst pellets are also exposed to mechanical stresses during transport and storage, as well as loading and operation of the reactor itself [10]. The possibility of mechanical failure of solid catalyst pellets and moreover its negative consequences are commonly known [11]. The breakage of catalyst pellets results in smaller, diversely shaped and sized particle fragments, which influence the local packed bed morphology. As a result, breakage of catalyst pellets can lead to a maldistribution of fluid flow and an increase in pressure drop, which in turn might lower the efficiency and, in serious cases, can cause the shutdown of the reactor [12]. Hence, the mechanical strength of catalyst pellets is a key parameter for the efficient and reliable application of solid catalysts [12,13]. Farsi et al. used finite-discrete element methods (FDEM) to successfully simulate the fragmentation behavior of single, complex shaped catalyst pellets and drew conclusions on possible effects of catalyst pellet failure on pressure drop [14].

The same authors used FDEM methods to generate realistic catalyst packings while evaluating the mechanical stresses acting upon the individual pellets [15]. Wu et al. performed experiments to quantify the effect of mechanical catalyst pellet failure on the pressure drop for a few different particle shapes by applying pressures, large enough to break the catalyst pellets, at top of the packed beds [16]. An increase in pressure drop with an increased amount of broken particles and fines generated was found [16]. However, a scientific model with which the pressure drop and the packed bed morphology with catalyst pellet fragments can be predicted, is still called for.

In this work, experiments are conducted to quantify the influence of catalyst pellet breakage on the overall void fraction and the pressure drop of packed beds with a tube-to-particle diameter ratio of $N = 4.4$. Steatite rings and their artificially created fragments are used to create the needed packed bed structures with specific portions of pellet breakage.

A novel method is presented that enables the generation of synthetic packed beds of catalyst pellets of arbitrary shape while considering catalyst pellet breakage. The method avoids modeling the computationally intense breakage process and instead relies on experimental data of particle fragments obtained by common pellet drop tests and two-dimensional characterization methods. Hence, the method can be used with reasonable prior experimental effort. Fundamentally, the method consists of three steps: The creation of digital particle fragments, the selection of a digital particle fragment collective suitable for the accurate description of the experimental particle fragment collective and the subsequent packed bed generation. Generated packed bed structures are validated using the obtained data for the overall void fraction ε as well as the pressure drop Δp of performed PRCFD simulations.

2. Methodology

The novel method presented in this work makes use of particle fragment data, to allow for the description of technically used catalyst systems. Instead of simulating the breakage of the pellets, particle fragments matching experimental data are selected prior to the generation of the packed bed. Chosen particle fragments are then added in place of intact particles. The packed bed generation is carried out in the open-source software Blender® 4.0.2.

2.1. Experimental setup and methods

Experiments were conducted to quantify the influence of catalyst pellet breakage on the packed bed morphology, especially the overall void fraction ε. Packed beds with a height h_F of 1.0 m were prepared in a polymethylmethacrylate tube with an inner diameter of 21.9 mm. The pellets used were rings made from steatite due to its high structural strength which prevents breakage when filling the tube. In order to implement their geometry into Blender®, the dimensions of 100 densely sintered, nonporous steatite rings with a total mass of 19.04 g were measured using the digital microscope *KEYENCE VHX-7000* and subsequent evaluation with the Python Library *OpenCV*. The rings feature an outer diameter of $d_{o,Ring} = (4.98 \pm 0.02)$ mm, an inner diameter $d_{i,Ring} = (2.56 \pm 0.02)$ mm and a height of $h_{Ring} = (5.07 \pm 0.10)$ mm. By multiplying the end face area of each ring with the respective height, its volume was determined. The density ρ_P of steatite was determined to 2612.45 kg m^{-3} by dividing the mass weighed by the total calculated volume. Fragments of these rings were generated manually which enables the creation of packed beds with specific breakage fractions w_B by mixing intact rings and fragments. A constant breakage fraction w_B throughout the entire bed height was aimed for. In practice this distribution was attempted by mixing small portions of rings and fragments before carefully dropping the mixture into the tube. The overall void fraction ε of the packed beds was determined using Eq. (1), in which ρ_P is the particle material density, $m_{P,total}$ the total particle mass and $h_{exp,total}$ the total height of the experimental packed bed.

$$\varepsilon = 1 - \frac{m_{P,total} \cdot \rho_P^{-1}}{\pi \cdot h_{exp,total} \cdot r_{i,Tube}^2} \tag{1}$$

Apart from the overall void fraction, the pressure drop across the packed beds was measured. As the pressure drop depends on the volumetric fluid flow, it is common practice to plot the pressure drop Δp versus the dimensionless particle Reynolds number Re_P, which is calculated by Eq. (2). The particle diameter d_P used in Eq. (2) equals the diameter of a sphere with the same specific surface as the rings and v_0 the superficial velocity. Combined with the density ρ_f and the dynamic viscosity η_f of air, the particle Reynolds number can be calculated:

$$Re_P = \frac{v_0 \cdot d_P \cdot \rho_f}{\eta_f} \tag{2}$$

The volumetric air flow was controlled by a *Brooks 5851S* mass flow controller and subsequently measured by a gas flow meter *Bronkhorst EL-FLOW Select F-111B*, which was set up to display the volumetric flow under standard conditions (0 °C, 1.013 bar). With a *Greisinger GTH 1150* thermometer (type K), the temperature of the air flow after the perfusion of the packed bed was measured. The measured temperature was then used to calculate the volumetric flow under standard conditions, which was needed to reach the desired volumetric flow of air. Using a *Greisinger GMH 3155*, the static overpressure in front of the packed bed was measured. For the calculation of the particle Reynolds number Re_P the dynamic viscosity $\eta_f = 18.55 \times 10^{-6}$ kg m^{-1} s at 25 °C and 1.0 bar and the density ρ_f of dry air derived from the ideal gas law was used.

2.2. Synthetic packed bed generation

2.2.1. Creation of digital particle fragment collectives

Geometry data of the desired catalyst pellet fragments is essential for their recreation in Blender®. For that reason, microscope images of the fragments are taken. After binarization using Otsu's thresholding method [17], the projection of each fragment can be extracted into a single image for separate analysis. Fig. 1 illustrates this part of the characterization workflow. In this work, all fragments were characterized regarding their perimeter U_{Br}, projection area A_{Br}, circularity Ψ_{Br} as well as the width $b_{Br,MAR}$ and length $l_{Br,MAR}$ of the minimal area rectangle (MAR) that surrounds the fragment projection. The circularity Ψ_{Br} is equal to the ratio of the perimeter of a circle of equal area to the actual perimeter of the fragment projection and can therefore be calculated by Eq. (3)[18].

$$\Psi_{Br} = \frac{\sqrt{4\pi A_{Br}}}{U_{Br}} \tag{3}$$

The shape of particle fragments is restricted by the physical dimensions of the intact particle. Hence, it is reasonable to generate catalyst pellet fragments by splitting the original pellet shape into segments. Using the Python application programming interface of Blender® and newly developed scripts, any pellet shape can be automatically broken down into circular and linear segments which enables the generation of large datasets of different fragments. Fig. 2 schematically illustrates both techniques as well as their combination. To ensure comparability, the catalyst pellet fragments generated using Blender® are characterized analogously to the experimental fragments, which requires saving an orthogonal image of the fragment projection from above. It is important to note that particle fragments have a favored position when laying on a flat surface. Hence, the digital particle fragments are dropped multiple times with different starting rotations and the position with the lowest center of mass is chosen for the top view image. The projection of each particle can be evaluated concerning arbitrary features such as area, perimeter, specific lengths or form factors. Matching digital and experimental fragments should yield equal values for any evaluated feature. The distribution of any feature of the digital and experimental

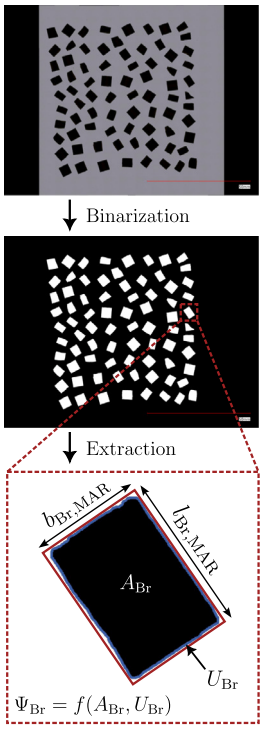

Fig. 1. Workflow of particle fragment characterization using microscope images and Python.

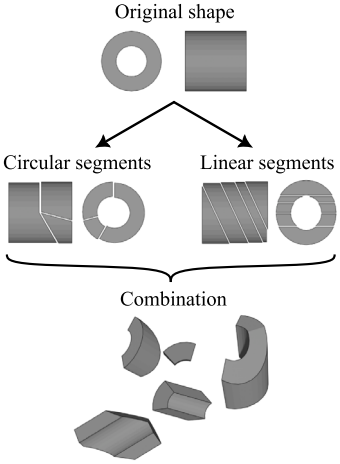

Fig. 2. Schematic depiction of the segmentation techniques used for fragment generation based on the original pellet shape in Blender®.

fragments must also be equal, if the fragments are equal. The goal of the particle selection is to choose a combination of particles that accurately describes all feature distributions simultaneously.

The combinatorial particle selection problem can be formulated as a general multidimensional knapsack problem (MDKP). A definition of the MDKP can be found in [19]. The MDKP considers a knapsack of m dimensions with each dimension i having a capacity of κ_i $(i = 1, \dots, m)$. There are n different objects that can be added to the knapsack. Each object j is available u_j times and requires a_{ij} units of the capacity of dimension i of the knapsack. Including a single copy of object j yields a reward of c_j. The objective is to maximize the total reward Z of the included items. With x_j being the number of object j in the knapsack, the problem can be stated as follows:

$$
\begin{aligned}
max \quad & Z = \sum_{j=1}^{n} c_j x_j \\
subject\ to \quad & \sum_{j=1}^{n} a_{ij} x_j \le \kappa_i, && i = 1, 2, \dots, m \\
& x_j \le u_j, && j = 1, 2, \dots, n \\
& x_j \ge 0, \quad x_j \in \mathbb{N}, && j = 1, 2, \dots, n
\end{aligned}
$$

To transform the problem of particle selection into a MDKP, the size classes of all evaluated distributions λ with their k_λ size classes are summarized into one knapsack with $m = \sum_\lambda k_\lambda$ dimensions. Each dimension i has a capacity κ_i which is equal to the number of experimental fragments belonging to this size class. It is $a_{ij} = 1$ if the digital fragment j belongs to dimension i and $a_{ij} = 0$ if not. All digital fragments are available infinitely ($u_j > \max \kappa_i$) and their reward is set to $c_j = 1$. It is also required that a digital fragment and its feature values must belong to size classes where fragments are present in the experimental counterpart. This must be true for all considered features for any digital fragment. Hence, digital fragments that do not meet this requirement are neglected.

Given these assumptions, a solution to the particle selection problem can be approximated using the PECH$_\alpha$ algorithm. The primal effective capacity heuristic (PECH), as introduced by Akçay et al. is a greedy-like, heuristic method that is intended to solve the general multidimensional knapsack problem [19]. The effective capacity $\bar{y}_j$ which is defined by $\min_i\{\lfloor \bar{\kappa}_i / a_{ij} \rfloor\}$ is of major importance for the PECH$_\alpha$ algorithm. Intuitively, the effective capacity $\bar{y}_j$ can be understood as the maximum amount of object j that can be added to the knapsack. Every iteration, the algorithm selects an object j^* from *set* E, that yields the largest attainable reward $c_j \cdot \bar{y}_j$ and commits a fraction α of its effective capacity to the knapsack. The coefficient α therefore determines the algorithms greediness. A brief explanation of Fig. 3 is given in the following:

Start

Step 1 Initialize decision variables $x_j = 0, \forall j$;
Initialize *set* $E = \{j \mid x_j = 0, \forall j\}$;
Initialize capacities of resources $\bar{\kappa}_i = \kappa_i, \forall i$;
Initialize upper bounds of decision variables $\bar{u}_j = u_j, \forall j$;

Step 2 Compute effective capacity for item j
$\bar{y}_j = \min_i\{\lfloor \frac{\bar{\kappa}_i}{a_{ij}} \rfloor : a_{ij} > 0\}, \forall j \in E$;
If $\bar{y}_j = 0, \forall j \in E$, go to End, otherwise go to 3.

Step 3 Compute $c_j \cdot \bar{y}_j, \forall j \in E$ and select $j^* = \arg\max_{j \in E}\{c_j \cdot \bar{y}_j\}$;

Step 4 Compute the increment of item j^*
$y_{j^*} = \min\{\bar{u}_{j^*}, \max\{1, \lfloor \alpha \bar{y}_{j^*} \rfloor\}\}$;

Step 5 Update the values of decision variables $x_{j^*} \leftarrow x_{j^*} + y_{j^*}$;
Update remaining capacities of constraints
$\bar{\kappa}_i \leftarrow \bar{\kappa}_i - a_{ij^*} \cdot y_{j^*}, \forall i$;
Update slacks of decision variables $u_{j^*} \leftarrow u_{j^*} + y_{j^*}$;
Update *set* E If $u_{j^*} = 0$ or $\alpha = 1, E \leftarrow E - \{j^*\}$;
If $E = \emptyset$, go to End; otherwise go to Step 2.

End

Fig. 3. PECH$_\alpha$ algorithm as introduced by Akçay et al. with adapted variable notation [19].

In **Step 1**, the decision variables x_j, which are equal to the number of times the object j was added to the solution, are set to zero. The *set* E which contains all possible objects, the knapsack capacities $\bar{\kappa}_i$ and the upper bounds of the decision variables $\bar{u}_j$ are initialized to their respective values. **Step 2** calculates the effective capacity $\bar{y}_j$ for each object j, which is used in **Step 3** to compute the maximum possible

reward $c_j \cdot \bar{y}_j$ and select object j^*. After calculating the increment of object j^* in **Step 4**, all information is updated in **Step 5** before returning to **Step 2** for the next iteration.

2.2.2. Rigid body approach in blender

Flaischlen and Wehinger have shown that rigid body simulations carried out in Blender® can offer significant calculation time advantages over the discrete element methods (DEM) often implemented in commercial software [6]. Rigid body simulations are based on the model concept of an idealized rigid body. For rigid bodies, the distance between points within and on the surface of the body always remains constant [20]. The motion of rigid bodies is described by the Newton–Euler equations [20]. The time rate of momentum change, the product of mass m and the translatoric velocity v, must be equal to the sum of all forces f acting on the rigid body:

$$f = \frac{d(mv)}{dt} \tag{4}$$

The net momentum τ is equal to the change of rotational momentum with time, whereas the rotational momentum itself is the product of the inertia matrix I and the angular velocity ω:

$$\tau = \mathrm{I}\dot{\omega} + \omega \times \mathrm{I}\omega \tag{5}$$

The usage of these equations for the simulation requires knowledge of the forces acting upon the respective rigid body to calculate f and τ. A contact of rigid bodies results in a contact force f_c acting upon both bodies at the contact point. Within the Coulomb friction model, the contact force f_c is decomposed into a normal component f_{nor}, as well as tangential components f_{tan} and f_{ort}. The tangential components lie in a plane defined by the normal direction $\hat{n}$ and the contact point C. The relative velocity v at the touching points of the bodies is decomposed analogously into a normal component v_{nor} and two tangential components v_{tan} and v_{ort}. Sliding occurs when $v_{nor} = 0$ and at least one tangential velocity is not equal to zero. Both objects separate if v_{nor}, which cannot be negative, is greater than zero. The Coulomb model describes friction based on a quadratic friction cone $\mathcal{F}(f_{nor}, \mu_{\mathrm{fric}})$. The contact force f_c must lie within the friction cone and, in case of sliding, the friction force must be directly on the boundary of the cone, opposing the direction of sliding. The friction cone is defined by Eq. (6), wherein the friction coefficient $\mu_{\mathrm{fric}} \geq 0$ is determined by multiplying the friction factors of the two colliding objects.

$$\mathcal{F}(f_{nor}, \mu_{\mathrm{fric}}) = \{\mu_{\mathrm{fric}}^2 f_{nor}^2 - f_{tan}^2 - f_{ort}^2 \geq 0, f_{nor} \geq 0\} \tag{6}$$

The tangential friction forces f_{tan} and f_{ort} that occur when sliding are defined by Eqs. (7) and (8), with the sliding speed β calculated by Eq. (9).

$$f_{tan} = -\mu_{\mathrm{fric}} f_{nor} \frac{v_{tan}}{\beta} \tag{7}$$

$$f_{ort} = -\mu_{\mathrm{fric}} f_{nor} \frac{v_{ort}}{\beta} \tag{8}$$

$$\beta = \sqrt{v_{tan}^2 + v_{ort}^2} \tag{9}$$

Blender® uses the Bullet Phyics Library (BPL) for rigid body simulations [21]. Fundamentally, the BPL differentiates between static, kinematic and dynamic rigid bodies. While static rigid bodies have zero mass and have a fixed position, dynamic rigid bodies possess a positive mass, and their motion is determined by the simulation. Kinematic rigid bodies are not relevant for the developed packed bed generation method.

The BPL offers the possibility to assign a different collision shape to every object, which does not necessarily coincide with the visual shape of the object. With *Convex Primitives* and the *Convex Hull* collision shape, the collision of convex geometries can be accurately and efficiently described. For arbitrary, non-convex geometries, the BPL offers the *Concave Triangle Mesh* collision shape. Data from Flaischlen and Wehinger shows that using *Concave Triangle Meshes* increases the computation time by 13 times compared to the *Convex Hull* collision shape for generating packed beds comparable to the ones in this work [6]. Nonetheless, it is necessary to use *Concave Triangle Meshes* for the realistic description of concave pellets and their often non-convex fragments.

2.2.3. Filling algorithm

Using the Blender® Python API [22], the packed bed generation is fully automated. A basic flowchart of the algorithm is illustrated in Fig. 4. The algorithm mimics the filling process by dropping single particles into the reactor volume and is based on previous work by Partopour and Dixon [23] as well as Kutscherauer et al. [24]. Individual particles are dropped into the reactor volume periodically until the final bed height or a specified number of particles is reached. Each particle is generated at a random position above the reactor opening which is restricted in a way that the drop results in a free fall without touching the reactor walls. After a certain amount of timesteps, the current bed height h_{current} is determined. To drastically improve calculation time and stability, particles below $h_{\mathrm{current}} - h_{\mathrm{dynamic}}$ are set to static rigid bodies, essentially freezing them, which removes the need to calculate their motion and therefore reduces simulation time [24].

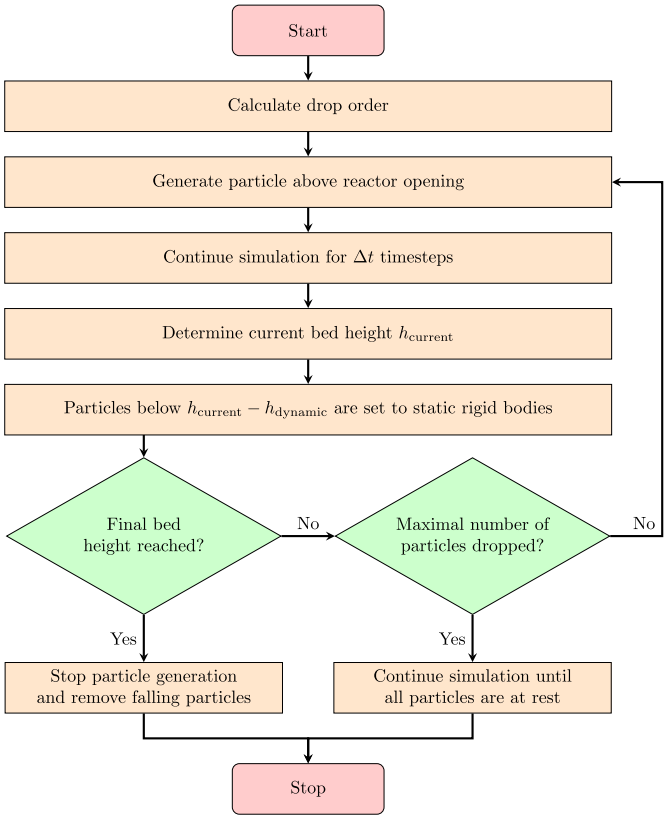

Fig. 4. Flowchart of the packed bed generation filling algorithm based on Kutscherauer [24].

Due to the multiple different geometries (particle and fragments) used, a method is needed to determine a suitable order in which the different shapes are dropped into the reactor. By choosing specific drop orders, the packed bed morphology can be strongly influenced. In this work, the drop order is chosen specifically to generate an axially homogeneous distribution of particle fragments. More precisely, a constant mass-related breakage fraction $w_{\mathrm{B}} = m_{\mathrm{B}}/m_{\mathrm{P,total}}$ across the entire bed height is aimed for. The friction coefficient for all particles was determined by matching the overall void fraction ε of breakage free, synthetically generated packed beds to the experimental data while all other parameters were held constant as suggested by Jurtz

et al. [25]. With the friction coefficient $\mu_{\text{Tube}} = 0.2$ for the tube wall and $\mu_{\text{P}} = 0.75$ for all particle surfaces, two constant values were used. The void fractions of the generated synthetic packed beds were determined via a ray-casting algorithm in Blender® as suggested by Partopour and Dixon [23].

To increase the performance and stability of the collision detection, the BPL uses an additional distance called *Collision Margin* that specifies the distance to the objects surface, in which a collision is detected. The *Collision Margin* can introduce a visible gap between objects when used in combination with the collision shape *Concave Triangle Mesh*. Hence, it is needed to set the *Collision Margin* of all particles to zero according to Partopour and Dixon [23]. While the authors agree with that, the *Collision Margin* of the wall can be used to drastically increase simulation stability while still maintaining the desired geometry. In the case of tubular reactors, this can be done by increasing the radius of the tube by the chosen *Collision Margin*.

2.3. Computational fluid dynamics

2.3.1. Governing equations

All CFD simulations were performed under isothermal, steady-state conditions. The simulations are governed by mass continuity and momentum conversation equations that are presented below. Detailed descriptions and explanations of the governing equations can be found in the relevant literature [26].

Mass continuity:

$$\nabla\cdot(\rho_{\text{f}}\mathbf{v}) = 0 \tag{10}$$

Conservation of momentum:

$$\nabla\cdot(\rho_{\text{f}}\mathbf{v}\otimes\mathbf{v}) = -\nabla p + \nabla\cdot\mathbf{T} \tag{11}$$

With the viscous stress tensor $\mathbf{T}$:

$$\mathbf{T} = \eta_{\text{f}}\mathbf{D} - \frac{2}{3}\eta_{\text{f}}\nabla\cdot\mathbf{v}\mathbf{e} \tag{12}$$

The deformation tensor $\mathbf{D}$ is defined as follows:

$$\mathbf{D} = \nabla\mathbf{v} + (\nabla\mathbf{v})^{\text{T}} \tag{13}$$

As equation of state, the ideal gas law was employed in order to describe the relationship between temperature, pressure and fluid density:

$$\rho_{\text{f}} = \frac{pM_{\text{f}}}{RT} \tag{14}$$

For $\text{Re}_{\text{P}} \geq 200$, the flow regime was considered to be turbulent as suggested by Ziółkowska et al. [27]. In turbulent flow regimes, the Reynolds Averaged Navier Stokes (RANS) approach was applied, specifically, the realizable k-ε turbulence model with the two layer all y^+ wall treatment of Siemens Simcenter STAR-CCM+ [28,29]. All simulations were performed on 20 cores of two Intel Xeon E5-2687W CPUs at 3.00 GHz on a system with 128 GiB of RAM running Ubuntu 22.04.5 LTS.

2.3.2. Contact modification and mesh generation

The meshing of packed bed structures for subsequent PRCFD was carried out in Siemens Simcenter STAR-CCM+ v2402 using built-in functionality. For each simulation a representative packed bed section with a length of $50d_{o,Ring}$ taken from the center of the generated structure was imported as an STL file. A tube with radius $d_{\text{i,Tube}}$ of 21.9 mm is introduced around the packed bed geometry. As commonly stated in literature, the particle–particle and particle–wall contacts provide major issues for the mesh generation prior to PRCFD, as mesh cells generated there can be of low quality [30,31]. Many authors use different contact modification methods to alter the geometry in proximity to the contacts to enable the generation of good quality mesh cells by the meshing algorithm in these regions, while guaranteeing physical accuracy [30–33]. Particle–wall contacts were modified by subtracting a tube with reduced radius from the entire packed bed geometry, in analogy to Kutscherauer et al. [34]. In this work, the tube used for the capping has a radius of $r_{\text{i,Tube}} - 0.01d_{\text{o,Ring}}$, which introduces a particle–wall gap of 1.0 % of the outer diameter of the ring $d_{\text{o,Ring}}$. The particle–particle contacts were modified using the "caps" method suggested by Eppinger et al. [35]. The particle surface near particle–particle contacts is locally flattened when the distance between two surfaces is below a specified minimum. This modification is performed by the automated meshing algorithm for surface meshes built into STAR-CCM+. A polyhedral core mesh with three prism layers around surfaces for accurate resolution of the boundary layer was chosen. As suggested by Kutscherauer et al. the number of prism layers was reduced at close proximity surfaces to avoid cells of poor quality [34]. The thickness of the momentum boundary layer δ_{BL} was approximated by Eq. (15) which is a correlation for the stagnation point on a sphere taken from the work by Dhole et al. [36]. The obtained value of $\delta_{\text{BL}} = 1.265 \times 10^{-4}$ m was subsequently used as prism layer total thickness to enable a sufficiently accurate resolution of the momentum boundary layer.

$$\frac{\delta_{\text{BL}}}{d_{\text{P}}} = 1.13\text{Re}_{\text{P}}^{-0.5} \tag{15}$$

Relevant settings used for the automated surface and volume mesh generation are listed in the supplementary material in Section S1.

2.3.3. Simulation setup

In the presented work, the influence of the breakage fraction w_{B} on the pressure drop of representative sections of packed beds was investigated for breakage fractions w_{B} of 0.0 and 0.1. For each breakage fraction, the flow was simulated through a section of a single packed bed with a length of $50d_{\text{o,Ring}}$. The inlet velocity was set by a function in order to maintain a particle Reynolds number Re_{P} corresponding to the experiments carried out.

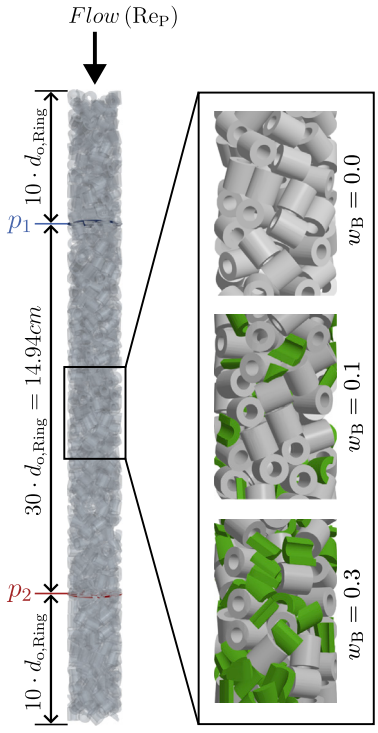

Fig. 5. Schematic illustration of the simulation setup with plane sections used for pressure drop determination highlighted and marked with p_1 and p_2. The insert shows three different bed sections with increasing breakage fraction (fragments colored green).

The outlet pressure was set to a constant value depending on the experimentally observed pressure drop, so that the fluid density at the inlet is approximately the same in the simulation and the experiment.

The outlet pressure value p_{out} was approximated by assuming a linear change of the pressure throughout the total experimental packed bed height $h_{exp,total}$, which leads to Eq. (16).

$$p_{out} = \frac{\Delta p_{exp}(Re_P, w_B)}{h_{exp,total}} h + p_0 \tag{16}$$

Since the simulated packed bed height was chosen to be $50 d_{o,Ring}$, Eq. (16) was evaluated at $h = h_{exp,total} - 50 d_{o,Ring} = 0.751$ m. Effectively, the first layers of the packed bed downstream from the tube inlet were simulated. In the simulation, the pressure drop was calculated as the difference of the average pressure of two planar sections. Both sections are highlighted in Fig. 5 and marked with p_1 and p_2 respectively. In the figure, the insert shows three different bed sections with increasing breakage fraction (fragments colored green).

3. Results and discussion

3.1. Particle selection results

In the following, the characterization results are discussed on the example of the width $b_{Br,MAR}$ and length $l_{Br,MAR}$ as they show important characteristics of the artificial particle fragments. Graphs for additional particle size features are added to the supporting information in Section S2. The particle size distribution (PSD) $q_0(l_{Br,MAR})$ of the experimental fragments shows a sharp distribution with a peak at $l_{Br,MAR} = 5.10$ mm, which is close to the intact rings height of $h_{Ring} = (5.07 \pm 0.10)$ mm. Since it is the only peak, almost all fragments must feature a length in that region. The PSD $q_0(b_{Br,MAR})$ on the other hand peaks at the size classes $b_{Br,MAR} = 3.54$ mm and $b_{Br,MAR} = 4.86$ mm, which could correspond to the projection area of a quarter and a half of a ring respectively. Visual examination of the real particle fragments confirms this hypothesis: the artificial fragments mainly consist of halves and quarters of intact rings. Therefore, the fragments boast a similar order of magnitude as the intact rings regarding their size.

A dataset of 18,000 digital fragments was created, of which 65.2 % were potential candidates for the particle selection, as all their size feature values fit into size classes also occupied by experimental fragments. Using a greedy coefficient of $\alpha = 0.05$, PECH$_\alpha$ yields a selection of 2584 particle fragments with 536 unique shapes that approximate the experimental particle collective.

By plotting the used capacity $\sigma_{i'}$ over the total capacity $\kappa_{i'}$, Fig. 6 illustrates the approximated particle selection solution and indicates how well certain size classes are represented by the selected digital fragments. For clarity reasons, only the dimensions i' with a capacity of more than 1.0 % of the largest dimensions capacity are plotted. Unused capacities can be attributed to two possibilities. The first possibility is that there was no fitting fragment for the given size class in the dataset. It is also possible that the remaining capacity $\overline{\kappa}_i$ was insufficient to add any of the potential candidate fragments.

Fig. 7 enables the visual comparison between the particle size distributions of the experimental and selected fragments. The PSD of the selected fragments shows larger values than the experimental fragments for size classes that belong to a peak of that feature in the experimental distribution. This can be directly attributed to the transformation of the particle selection problem into a MDKP and the selection of fragments by the PECH$_\alpha$ algorithm. In each iteration, the algorithm chooses the fragment j that leads to the largest increase in total value $c_j \cdot \overline{y}_j$. Since the value c_j is set to 1 for all fragments, the effective capacity $\overline{y}_j$ is decisive. The effective capacity $\overline{y}_j$, on the other hand depends on the remaining capacity $\overline{\kappa}_i$ and the respective unit requirement a_{ij}, which was set to 1 for all dimensions i and fragments j in this work. Hence, the remaining capacity $\overline{\kappa}_i$ is equal to the number fragments that can be added to dimension i. Any fragment belongs to λ dimensions i, with λ being equal to the number of particle size features used for the fragment selection. The smallest remaining capacity $\overline{\kappa}_i$ among the λ concerning dimensions is decisive for the selection of the fragment. This automatically leads to the constraint that all the other remaining capacities of the other dimensions must be larger. The dimensions with the largest capacities are filled up preferably given that there are fitting fragments in the dataset. As a consequence, fragment shapes that belong to the peaks appear over proportionately. However, the distributions of the characteristic fragment parameter of the fragment collection selected by the PECH$_\alpha$ algorithm agree well with the experimentally determined distributions.

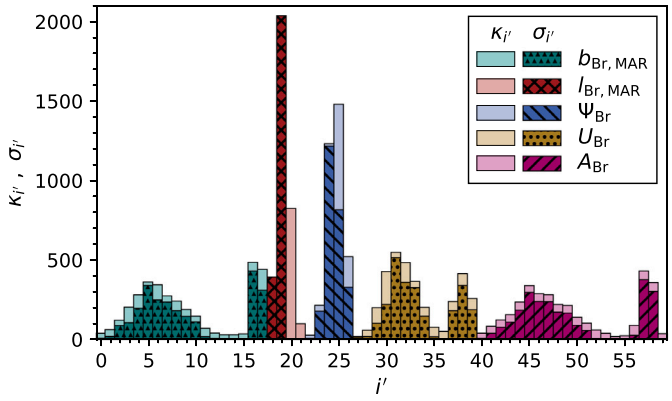

Fig. 6. Capacity $\kappa_{i'}$ and used capacity $\sigma_{i'}$ of the approximated particle selection solution. Only dimensions i' with a capacity of $\kappa_{i'} > 0.01 \cdot \max(\kappa_i) \forall i$ are shown.

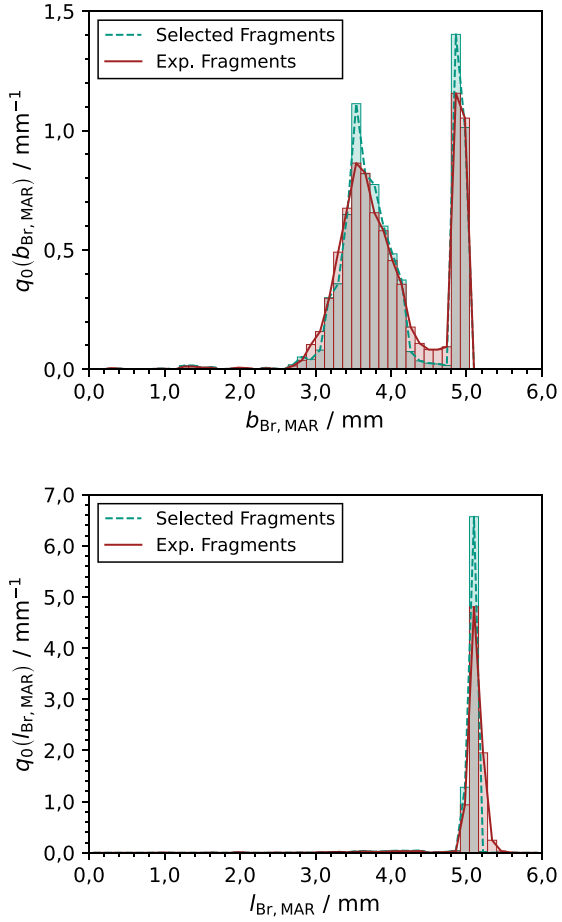

Fig. 7. Particle size distribution related to particle count $q_0(b_{Br,MAR})$ and $q_0(l_{Br,MAR})$ of the experimental artificial fragments and the selected digital fragments.

3.2. Packed bed morphology

As depicted in Fig. 8 the breakage fraction w_B has significant impact on the overall void fraction ε. For each datapoint three packed beds were generated and the respective mean value is plotted. The packed beds generated synthetically reflect the decrease in the void fraction with an increase in the breakage fraction w_B that is present in the experimental data. The overall void fraction of the synthetically generated packed beds at $w_B = 0.0$ was matched to the experimental data by adjusting the particle friction coefficient μ_P. Packed beds at larger breakage fractions were calculated using identical friction coefficients. With increasing breakage fraction, an increasing deviation from the experimental data is found. The synthetically generated packed beds show an increased overall void fraction compared to the experimental packed beds. With increasing breakage fraction, the number of objects in the dynamic particle layer increases. This leads to an overall increase in particle contacts, which inevitably causes contact forces. As a result, particles perform small movements around their position, enlarging the mean distance to neighboring particles and thereby raising the overall void fraction. An increase in movement with increasing breakage fraction can also be observed visually during the simulation. Apart from that, the characterization method is restricted to two-dimensional images and therefore cannot fully capture the three-dimensional geometric data. Further, the particle selection algorithm is biased towards the peak size classes. Fragments belonging to a combination of size classes with large capacity κ_i are preferred, which must not necessarily be a size feature combination found as commonly in the experimental fragment data. Yet, the overall void fraction of the synthetically generated packed beds shows a maximum deviation of less than 2 % at $w_B = 0.3$.

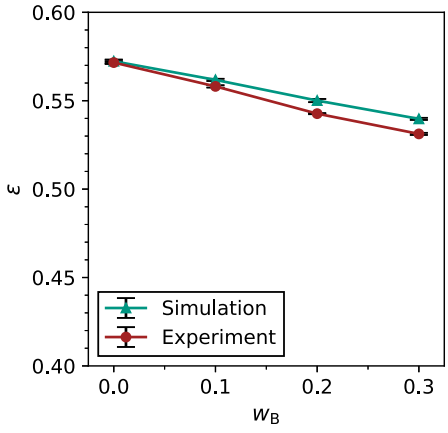

Fig. 8. Overall void fraction ε of the experimental and synthetically generated packed beds with varying breakage fraction w_B.

Local void fraction profiles highly depend on the particle shape [37]. Pellet fragments can close gaps between intact pellets, introduce additional distance between them and affect their position and orientation. Therefore, an influence of catalyst pellet breakage on local packed bed structure is expected. The local void fraction $\varepsilon(r)$ of the generated packed beds show local minima and maxima depending on the distance to the tube wall, as depicted in Fig. 9. In the presented case, local minima and maxima are reduced with increasing breakage fraction w_B and a radially more uniform void fraction is achieved. The standard deviation in radial void fraction $\varepsilon(r)$ is shown as a filled area around the lines in Fig. 9. The deviation between individual generated packed beds of a specific breakage fraction is most pronounced in the center of the tube. Section S3 of the supplementary information provides additional information about the positioning of rings and fragments over the cross-sectional area of the tube.

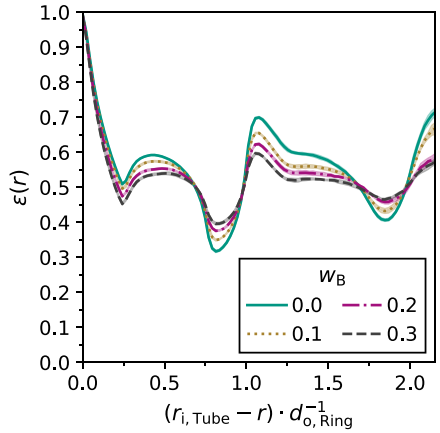

Fig. 9. Mean radial void fraction $\varepsilon(r)$ of synthetically generated packed beds and their standard deviation (filled area around curve) at different breakage fractions w_B plotted over the dimensionless radius $(r_{i,Tube} - r) \cdot d_{o,Ring}^{-1}$.

3.3. Pressure drop

Fig. 10 shows the mean value of the pressure drop Δp of three different experimental packed beds with an axially homogeneous breakage distribution at various breakage fractions w_B and different particle Reynolds numbers Re_P. With increasing breakage fraction w_B, the pressure drop also steadily increases for the examined particle system. Compared to the breakage-free packed bed, the packed bed configuration at $w_B = 0.1$ yields a pressure drop increase of 21.2 % at $Re_P = 411$. This shows that already minor breakage fractions can lead to a significant increase in pressure drop and therefore to an increased energy consumption for gas compression or reduced flow rates at constant pressure drop.

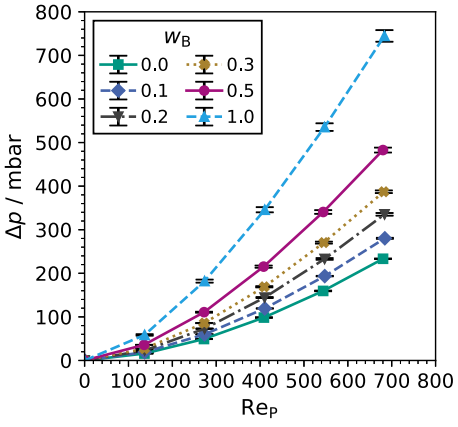

Fig. 10. Pressure drop Δp of experimental fixed beds with different breakage fractions w_B and axially homogeneous breakage distribution at different particle Reynolds numbers Re_P.

PRCFD simulations were conducted of three packed beds with $w_B = 0.0$ (reproducibility) and single packed beds with $w_B = 0.1$ and $w_B = 0.3$ respectively for all experimentally investigated particle Reynolds numbers Re_P. The void fraction of the generated packed beds without breakage ($w_B = 0.0$) show a relative standard deviation of 0.172 %, which was the highest value across all investigated breakage fractions. The numerical pressure drop values of the packed beds without pellet breakage show a relative standard deviation of less than 1.684 %. Hence, it is sufficient to simulate one of the respective packed beds for a given breakage fraction to quantify the pressure drop of a given packed bed. With increasing particle Reynolds numbers Re_P and

increasing breakage fractions w_B, the simulated length normalized pressure drop increases, see Fig. 11. The simulated specific pressure drop deviates less than 10 % from the experimentally measured values, as can be seen in the parity plot in Fig. 11(b). The scattering of the deviations between −10 % and +10 % indicates that there is no systematic error in the model. Possible sources of deviation are associated with particle orientation, as well as fragment position, orientation and agglomeration. This could be further investigated using extensive image-based analysis (e.g. tomography) of experimental beds. The observed small differences between simulation and experiment are inevitable since the simulation did not cover the whole packed bed structure. Since the fluid density is different in the first particle layers compared to the last layers, the velocities and the pressure drop per meter packed bed change over the packed bed as well. This is especially critical if the fluid density is not adjusted according to the actual experimental conditions, which was done in this work by adjusting the outlet pressure.

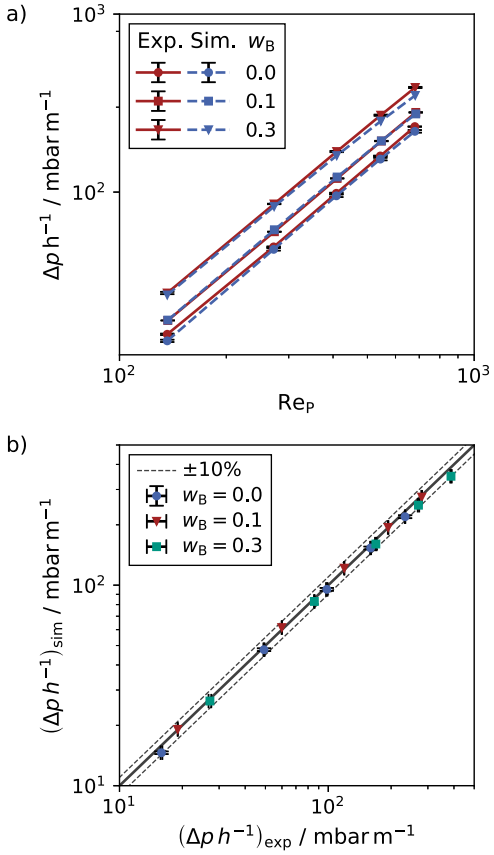

Fig. 11. Pressure drop of experimental and synthetic packed beds over particle Reynolds number Re_P (a) and as a parity plot (b).

Fig. 12 provides a visual representation of the fluid flow through packed beds at three different breakage fractions and $Re_P = 411$. The particle fragments are green for visualization purposes only. A small section of the packed beds and its near-wall streamlines (top) and plane sections with the axial velocity (bottom) are shown. It is visible that pellet fragments can locally hinder the axial fluid flow which can be seen in the case of fragments close to the tube wall at $w_B = 0.3$. From the plane sections it is clear that the local axial velocity increases with increasing breakage fraction, which is expected with the lower overall void fraction. The increased flow deflection leads to a higher pressure drop.

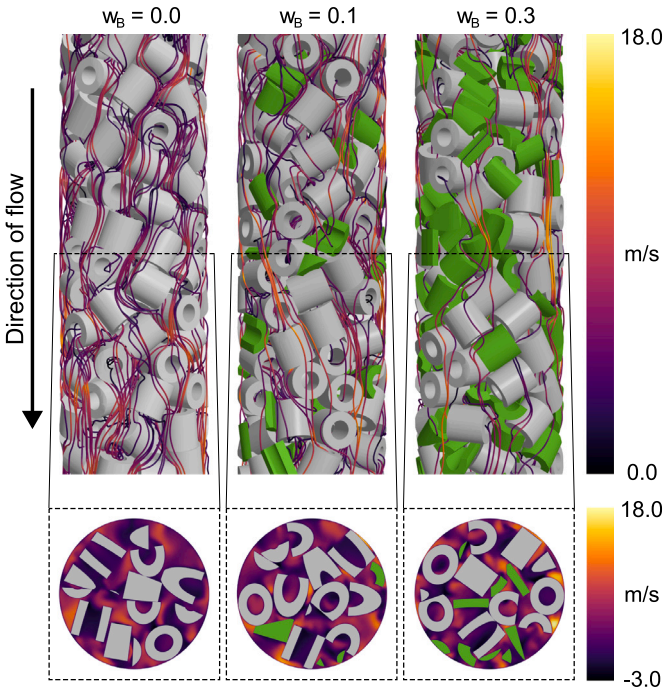

Fig. 12. Streamlines (velocity magnitude) and axial velocity in plane sections of packed beds with different breakage fractions at $Re_P = 411$ and equal height.

4. Conclusion

The centerpiece of any packed bed reactor is the bed made of solid catalyst, which provides the main site for chemical reactions. Mechanical stresses arising during loading and operation of the reactor can lead to the failure of the employed catalyst pellets. The subsequent change of the packed bed morphology inevitably affects the reactor performance.

It has been confirmed experimentally that catalyst pellet breakage has significant influence on the packed bed morphology. Packed beds made of inert rings and their fragments were investigated. Overall, the fragments were mainly halves and quarters of intact rings and, therefore, had sizes of similar order of magnitude. Nonetheless, with increasing breakage fraction, a decrease of the overall void fraction and the expected pressure drop increase were observed. In the investigated case, a breakage fraction w_B of 10 % already results in an increase of pressure drop of more than 20 %, which shows the importance of considering catalyst pellet fragments.

Simulative investigation of the influence of packed bed morphology on reactor performance, for example by PRCFD, requires a digital replica of the packed bed. A novel method for the generation of packed beds considering catalyst pellet fragments for arbitrary catalyst pellet shapes has been developed, which does not require expensive equipment compared to image-based experimental methods. The novel method consists of the creation, characterization and selection of digital fragments. Starting from the original catalyst pellet shape, a set of particle fragments is created and characterized in Blender®. Using the PECH$_\alpha$ algorithm, a suitable digital particle fragment collection, matching experimental particle fragment data, is selected for the subsequent packed bed generation using Blender®.

The void fraction of experimentally and synthetically generated packed beds shows very good agreement in the technically relevant breakage fraction range of $0.0 \leq w_B \leq 0.3$ with a maximum deviation of less than 2 %. The pressure drop of packed beds with a breakage fraction of $w_B = 0.0, 0.1, 0.3$, was investigated with PRCFD. Good agreement between experimental and simulative pressure drop values was found,

with a deviation of less than 10 % for all examined breakage fractions w_B and particle Reynolds numbers Re_P. It is important to note that, in addition to the geometric information and breakage distribution, no further experimental information is required for predicting the void fraction and pressure drop.

The presented method lays the foundation for further simulative investigations of the effects of catalyst pellet breakage on reactor performance. A more realistic depiction of the packed bed morphology enables an improved description of the local flow field. Investigating industrial reactors will enhance the understanding of how catalyst pellet breakage affects pressure drop, chemical reactions, and local temperature profiles within the reactor. These insights can contribute to the optimized design of future reactors and catalyst pellet structures, and assist in making informed decisions regarding the timely replacement of catalyst beds in existing operations.

Future studies should examine particles and fragments of various geometries and validate the proposed method accordingly. Moreover, coupling the presented approach with FDEM-based simulations of catalyst pellet fragmentation, such as the model developed by Farsi et al. [14], is expected to eliminate the need for experimental fragmentation analysis.

CRediT authorship contribution statement

Maximilian Meyer: Writing – original draft, Visualization, Validation, Methodology, Investigation, Formal analysis, Data curation, Conceptualization. **Martin Kutscherauer:** Writing – review & editing, Writing – original draft, Supervision, Methodology, Conceptualization. **Oliver Richter:** Writing – review & editing, Resources, Methodology, Investigation, Data curation. **Maximilian Dochnahl:** Writing – review & editing, Supervision, Resources, Conceptualization. **Gerhard Mestl:** Writing – review & editing, Supervision, Resources, Methodology, Formal analysis, Conceptualization. **Gregor D. Wehinger:** Writing – review & editing, Writing – original draft, Supervision, Methodology, Conceptualization.

Declaration of competing interest

The authors declare that they have no known competing financial interests or personal relationships that could have appeared to influence the work reported in this paper.

Appendix A. Supplementary data

Figure data and simulated packed bed structures are available online at https://doi.org/10.5281/zenodo.17553745.

Supplementary material related to this article can be found online at https://doi.org/10.1016/j.powtec.2025.121957.

Data availability

Data is available from the authors upon request.

References

[1] A.A. Shaikh, Heterogeneous Catalysis: Solid Catalysts, Kinetics, Transport Effects, Catalytic Reactors, De Gruyter, 2023, pp. 2–3, http://dx.doi.org/10.1515/9783111032511.

[2] P. Andrigo, R. Bagatin, G. Pagani, Fixed bed reactors, Catal. Today 52 (2) (1999) 197, http://dx.doi.org/10.1016/S0920-5861(99)00076-0.

[3] G. Eigenberger, W. Ruppel, Catalytic fixed-bed reactors, in: Ullmann's Encyclopedia of Industrial Chemistry, John Wiley & Sons, Ltd, 2012, pp. 1–17, http://dx.doi.org/10.1002/14356007.b04_199.pub2.

[4] M. Kutscherauer, P. Reinold, S. Böcklein, G. Mestl, T. Turek, G.D. Wehinger, How temperature measurement impacts pressure drop and heat transport in slender fixed beds of raschig rings, ACS Eng. Au 3 (1) (2023) 45–58, http://dx.doi.org/10.1021/acsengineeringau.2c00039.

[5] N. Jurtz, M. Kraume, G.D. Wehinger, Advances in fixed-bed reactor modeling using particle-resolved Computational Fluid Dynamics (CFD), Rev. Chem. Eng. 35 (2) (2019) 139–190, http://dx.doi.org/10.1515/revce-2017-0059.

[6] S. Flaischlen, G.D. Wehinger, Synthetic packed-bed generation for CFD simulations: Blender vs. STAR-CCM+, ChemEngineering 3 (2) (2019) 17–18, http://dx.doi.org/10.3390/chemengineering3020052.

[7] J.-P. Latham, J. Xiang, A. Farsi, C. Joulin, N. Karantzoulis, A class of particulate problems suited to FDEM requiring accurate simulation of shape effects in packed granular structures, Comput. Part. Mech. 7 (5) (2020) 975–986, http://dx.doi.org/10.1007/s40571-019-00294-5.

[8] Z. Wang, A. Afacan, K. Nandakumar, K.T. Chuang, Porosity distribution in random packed columns by gamma ray tomography, Chem. Eng. Process.: Process. Intensif. 40 (3) (2001) 209–219, http://dx.doi.org/10.1016/S0255-2701(00)00108-2.

[9] M.J. Baker, P.G. Young, G.R. Tabor, Image based meshing of packed beds of cylinders at low aspect ratios using 3d MRI coupled with computational fluid dynamics, Comput. Chem. Eng. 35 (10) (2011) 1969–1977, http://dx.doi.org/10.1016/j.compchemeng.2011.03.017.

[10] D. Wu, J. Zhou, Y. Li, Mechanical strength of solid catalysts: Recent developments and future prospects, AIChE J. 53 (10) (2007) 2618–2619, http://dx.doi.org/10.1002/aic.11291.

[11] E. Gallei, E. Schwab, Development of technical catalysts, Catal. Today 51 (3) (1999-07-29) 535–539, http://dx.doi.org/10.1016/S0920-5861(99)00039-5.

[12] Y. Li, D. Wu, J. Zhang, L. Chang, D. Wu, Z. Fang, Y. Shi, Measurement and statistics of single pellet mechanical strength of differently shaped catalysts, Powder Technol. 113 (1) (2000) 176, http://dx.doi.org/10.1016/S0032-5910(00)00231-X.

[13] E. David, Mechanical strength and reliability of the porous materials used as adsorbents/ catalysts and the new development trends, Arch. Mater. Sci. Eng. 73 (1) (2015) 6–7.

[14] A. Farsi, J. Xiang, J.P. Latham, M. Carlsson, E.H. Stitt, M. Marigo, Strength and fragmentation behaviour of complex-shaped catalyst pellets: *A numerical and experimental study*, Chem. Eng. Sci. 213 (2020) 1–18, http://dx.doi.org/10.1016/j.ces.2019.115409.

[15] A. Farsi, J. Xiang, J.-P. Latham, M. Carlsson, H. Stitt, M. Marigo, Packing simulations of complex-shaped rigid particles using FDEM: *An application to catalyst pellets*, Powder Technol. 380 (2021) 443–461, http://dx.doi.org/10.1016/j.powtec.2020.11.010.

[16] D. Wu, L. Song, B. Zhang, Y. Li, Effect of the mechanical failure of catalyst pellets on the pressure drop of a reactor, Chem. Eng. Sci. 58 (17) (2003) 3995–4004, http://dx.doi.org/10.1016/S0009-2509(03)00286-0.

[17] N. Otsu, A threshold selection method from gray-level histograms, IEEE Trans. Syst. Man, Cybern. 9 (1) (1979-01) 62–66, http://dx.doi.org/10.1109/TSMC.1979.4310076.

[18] M. Stieß, Mechanische Verfahrenstechnik - Partikeltechnologie 1, in: Springer-Lehrbuch, Springer, Berlin, Heidelberg, 2009, p. 19, http://dx.doi.org/10.1007/978/3-540-32552-9.

[19] Y. Akçay, H. Li, S.H. Xu, Greedy algorithm for the general multidimensional knapsack problem, Ann. Oper. Res. 150 (1) (2007) 17–29, http://dx.doi.org/10.1007/s10479-006-0150-4.

[20] J. Bender, K. Erleben, J. Trinkle, Interactive simulation of rigid body dynamics in computer graphics, Comput. Graph. Forum 33 (1) (2014) 246–270, http://dx.doi.org/10.1111/cgf.12272.

[21] E. Coumans, Bullet 2.83 Physics SDK Manual (2015), 2025, https://github.com/bulletphysics/bullet3/blob/master/docs/Bullet_User_Manual.pdf. (Accessed on 24 April 2025).

[22] Blender 4.0 Python API Documentation (2024), 2025, https://docs.blender.org/api/4.0/. (Accessed on 20 May 2025).

[23] B. Partopour, A.G. Dixon, An integrated workflow for resolved-particle packed bed models with complex particle shapes, Powder Technol. 322 (2017) 261–263, http://dx.doi.org/10.1016/j.powtec.2017.09.009.

[24] M. Kutscherauer, Particle-Resolved CFD Simulation of Catalytic Fixed Bed Reactors for Maleic Anhydride Production (Ph.D. thesis), Clausthal University of Technology, 2024, http://dx.doi.org/10.21268/20240522-0.

[25] N. Jurtz, P. Waldherr, M. Kraume, Numerical analysis of the impact of particle friction on bed voidage in fixed-beds, Chem. Ing. Tech. 91 (9) (2019) 1260–1266, http://dx.doi.org/10.1002/cite.201800190.

[26] H.A. Jakobsen, Chemical Reactor Modeling: Multiphase Reactive Flows, Springer International Publishing, 2014, http://dx.doi.org/10.1007/978-3-319-05092-8.

[27] I. Ziółkowska, D. Ziółkowski, Fluid flow inside packed beds, Chem. Eng. Process.: Process. Intensif. 23 (3) (1988) 137–164, http://dx.doi.org/10.1016/0255-2701(88)80012-6.

[28] T.-H. Shih, W.W. Liou, A. Shabbir, Z. Yang, J. Zhu, A new *k-varepsilon* eddy viscosity model for high reynolds number turbulent flows, Comput. & Fluids 24 (3) (1995) 227–238, http://dx.doi.org/10.1016/0045-7930(94)00032-T.

[29] Siemens Digital Industries Software, Simcenter STAR-CCM+ 2402 User Guide, 2024, pp. 4437–4441.

[30] A.G. Dixon, B. Partopour, Computational fluid dynamics for fixed bed reactor design, Annu. Rev. Chem. Biomol. Eng. 11 (2020) 109–130, http://dx.doi.org/10.1146/annurev-chembioeng-092319-075328.

[31] G.D. Wehinger, C. Fütterer, M. Kraume, Contact modifications for CFD simulations of fixed-bed reactors: Cylindrical particles, Ind. Eng. Chem. Res. 56 (1) (2017) 87–99, http://dx.doi.org/10.1021/acs.iecr.6b03596.
[32] S. Ookawara, M. Kuroki, D. Street, K. Ogawa, High-fidelity DEM-CFD modeling of packed bed reactors for process intensification, in: Proceedings of European Congress of Chemical Engineering, ECCE-6, 2007.
[33] A. Guardo, M. Coussirat, M.A. Larrayoz, F. Recasens, E. Egusquiza, CFD flow and heat transfer in nonregular packings for fixed bed equipment design, Ind. Eng. Chem. Res. 43 (22) (2004) 7049–7056, http://dx.doi.org/10.1021/ie034229+.
[34] M. Kutscherauer, S. Böcklein, G. Mestl, T. Turek, G.D. Wehinger, An improved contact modification routine for a computationally efficient CFD simulation of packed beds, Chem. Eng. J. Adv. 9 (2022) http://dx.doi.org/10.1016/j.ceja.2021.100197.
[35] T. Eppinger, K. Seidler, M. Kraume, DEM-CFD simulations of fixed bed reactors with small tube to particle diameter ratios, Chem. Eng. J. 166 (1) (2011) 324–331, http://dx.doi.org/10.1016/j.cej.2010.10.053.
[36] S.D. Dhole, R.P. Chhabra, V. Eswaran, A numerical study on the forced convection heat transfer from an isothermal and isoflux sphere in the steady symmetric flow regime, Int. J. Heat Mass Transfer 49 (5) (2006) 984–994, http://dx.doi.org/10.1016/j.ijheatmasstransfer.2005.09.010.
[37] J. von Seckendorff, O. Hinrichsen, Review on the structure of random packed-beds, Can. J. Chem. Eng. 99 (S1) (2021) 703–733, http://dx.doi.org/10.1002/cjce.23959.